The Journal of Chemical Physics

Rotationally inelastic scattering of OH by molecular hydrogen: Theory and experiment

Cite as: J. Chem. Phys. **142**, 204310 (2015); https://doi.org/10.1063/1.4921562
Submitted: 20 March 2015 . Accepted: 12 May 2015 . Published Online: 29 May 2015

H. Christian Schewe, Qianli Ma (马千里), Nicolas Vanhaecke, Xingan Wang (王兴安), Jacek Kłos, Millard H. Alexander, Sebastiaan Y. T. van de Meerakker, Gerard Meijer, Ad van der Avoird, and Paul J. Dagdigian

Rotationally inelastic scattering of OH by molecular hydrogen: Theory and experiment

H. Christian Schewe,[1,a)] Qianli Ma (马千里),[2,b)] Nicolas Vanhaecke,[1,3,c)] Xingan Wang (王兴安),[1,4] Jacek Kłos,[5] Millard H. Alexander,[5,6] Sebastiaan Y. T. van de Meerakker,[7] Gerard Meijer,[1,d)] Ad van der Avoird,[8,e)] and Paul J. Dagdigian[2,f)]

[1]*Fritz-Haber-Institut der Max-Planck-Gesellschaft, Faradayweg 4-6, D-14195 Berlin, Germany*
[2]*Department of Chemistry, The Johns Hopkins University, Baltimore, Maryland 21218-2685, USA*
[3]*Laboratoire Aimé Cotton-UMR 9188 CNRS, Université Paris-Sud 11 and Ecole Normale Supérieure Cachan, 91405 Orsay, France*
[4]*Department of Chemical Physics, University of Science and Technology of China, Hefei 230026, China*
[5]*Department of Chemistry and Biochemistry, University of Maryland, College Park, Maryland 20742-2021, USA*
[6]*Institute for Physical Science and Technology, University of Maryland, College Park, Maryland 20742-2021, USA*
[7]*Molecular and Laser Physics, Institute for Molecules and Materials, Radboud University Nijmegen, Heyendaalseweg 135, 6265 AJ Nijmegen, The Netherlands*
[8]*Theoretical Chemistry, Institute for Molecules and Materials, Radboud University Nijmegen, Heyendaalseweg 135, 6265 AJ Nijmegen, The Netherlands*

(Received 20 March 2015; accepted 12 May 2015; published online 29 May 2015)

We present an experimental and theoretical investigation of rotationally inelastic transitions of OH, prepared in the $X^2\Pi$, v = 0, $j = 3/2$ $F_1 f$ level, in collisions with molecular hydrogen (H_2 and D_2). In a crossed beam experiment, the OH radicals were state selected and velocity tuned over the collision energy range 75–155 cm^{-1} using a Stark decelerator. Relative parity-resolved state-to-state integral cross sections were determined for collisions with normal and *para* converted H_2. These cross sections, as well as previous OH–H_2 measurements at 595 cm^{-1} collision energy by Schreel and ter Meulen [J. Chem. Phys. **105**, 4522 (1996)], and OH–D_2 measurements for collision energies 100–500 cm^{-1} by Kirste *et al.* [Phys. Rev. A **82**, 042717 (2010)], were compared with the results of quantum scattering calculations using recently determined *ab initio* potential energy surfaces [Ma *et al.*, J. Chem. Phys. **141**, 174309 (2014)]. Good agreement between the experimental and computed relative cross sections was found, although some structure seen in the OH($j = 3/2$ $F_1 f \rightarrow j = 5/2$ $F_1 e$) + H_2($j = 0$) cross section is not understood. © *2015 AIP Publishing LLC.* [http://dx.doi.org/10.1063/1.4921562]

I. INTRODUCTION

There has been considerable interest in rotationally inelastic and reactive collisions of the OH radical. This radical is a key intermediate in combustion chemistry[1,2] and is an important atmospheric and astrophysical molecule.[3,4] Collisions of OH with the hydrogen molecule represent the simplest molecule-molecule collision involving this free radical. The rate constant for the OH + $H_2 \rightarrow H_2O$ + H reaction is small at room temperature [6.7×10^{-15} cm^3 $molecule^{-1}$ s^{-1} [5]], and the dominant collision process at room temperature and below is rotational inelasticity.

There have been a number of experimental studies of rotationally inelastic collisions of OH with rare gases and with the hydrogen molecule. Mostly, these have been crossed beam studies with laser fluorescence excitation to detect the rotational levels of the scattered OH. Recently, resonance-enhanced multiphoton ionization (REMPI) has been employed to measure differential cross sections for OH–He/Ar collisions.[6] Andresen and co-workers were the first to measure relative state-to-state integral cross sections for collisions of OH with H_2.[7,8] They employed a supersonically cooled OH beam, which prepared an equal population in the two Λ-doublet states of the lowest rotational level ($j = 3/2$ F_1). Schreel and ter Meulen[9] measured Λ-doublet resolved integral cross sections for OH–*para*-/normal-H_2 collisions with the help of an electrostatic state selector to prepare the $j = 3/2$ $F_1 f$ initial level. Kirste *et al.*[10] employed a Stark decelerator[11] to measure the dependence of the state-to-state integral cross sections out of this initial level upon the collision energy for OH–D_2 collisions. In this paper, we present new measurements of OH–H_2 integral cross sections, measured with the use of a similar Stark decelerator.

a)Electronic mail: schewe@fhi-berlin.mpg.de
b)Present address: Institut für Theoretische Chemie, Universtät Stuttgart, Pfaffenwaldring 55, D-70569 Stuttgart, Germany.
c)Present address: European Patent Office, Patentlaan 2, 2288 EE Rijswijk, The Netherlands.
d)Present address: Radboud University Nijmegen, 6265 AJ Nijmegen, The Netherlands.
e)Electronic mail: A.vanderAvoird@theochem.ru.nl
f)Electronic mail: pjdagdigian@jhu.edu

Concurrently, there has been considerable interest in the calculation of OH–H_2 state-to-state inelastic cross sections, motivated by importance of this process in astrophysics.[12–20] These calculations have employed potential energy surfaces (PES's) which have become increasingly accurate due to a more complete treatment of electron correlation.[20–22] Because of the orbital degeneracy of OH($X^2\Pi$), two PES's are required to describe the molecule-molecule interaction. For general OH–H_2 geometries, for which there is no plane of symmetry, the two electronic states belong to the same irreducible representation, which poses additional challenges in the quantum chemical calculations.

To avoid these complications, Kochanski and Flower (KF)[23] and Miller *et al.*[20] calculated OH–H_2 interaction energies at nuclear geometries possessing a plane of symmetry, so that the two states have different symmetries (A' and A''). These workers employed a self-consistent field (SCF) calculation with dynamic correlation described respectively by a perturbation correction and within the coupled electron-pair approximation. By contrast, Offer and van Hemert (OvH)[22] employed a multi-configuration self-consistent field method with corrections for the dispersion interaction to calculate electronically adiabatic PES's even for geometries lacking a plane of reflection symmetry. They then used a direct calculation of the adiabatic-diabatic mixing angle.

In a recent work,[24] we used two methods for the calculation of the OH–H_2 PES's: multi-reference configuration interaction method [MRCISD+Q(Davidson)] and explicitly correlated spin-restricted coupled-cluster method with single-, double-, and (perturbative) triple excitations [RCCSD(T)-F12a]. The former method is applicable for any nuclear geometry while the latter requires a plane of symmetry but allows a more complete treatment of electron correlation. We showed that the coupled-cluster PES's provide an accurate description of the OH–H_2 interaction, despite the restricted angular sampling. In particular, for both sets of PES's, bound-state calculations of the dissociation energies (D_0) of the OH–*ortho*-H_2 and OH–*para*-D_2 complexes agreed well with experimental measurements.[25]

In this paper, we report new experimental measurements as well as calculations, based on our new PES's,[24] of state-to-state cross sections for OH–H_2 rotationally inelastic collisions. The range of collision energies investigated was lower than in the previous study of OH–D_2 collisions,[10] which also employed a Stark decelerator[11] to vary the collision energy. We also increased the resolution in collision energy to search specifically for resonance features[26–28] in the energy dependence of the cross sections. Overall, we find very good agreement of measured and computed state-to-state relative cross sections.

This paper is organized as follows: We briefly describe in Sec. II the methodologies employed in the experimental measurements and calculation of the cross sections for rotationally inelastic collisions. We compare in Sec. III A our computed cross sections with those computed by Offer *et al.*[19] at collision energies ranging from 5 to 500 cm^{-1}. Sec. III B presents our new measurements and calculations of state-to-state cross sections as a function of the collision energy for OH–H_2 scattering, while calculations of energy-dependent OH–D_2 cross sections are reported in Sec. III C and compared with the experimental measurements by Kirste *et al.*[10] The paper concludes with a discussion.

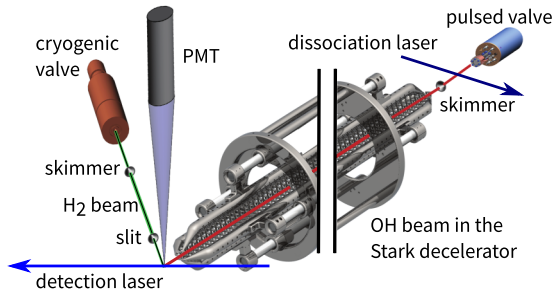

FIG. 1. This schematic drawing of the experimental apparatus shows the production and manipulation of the OH (red line) and H_2 (green line) packets before they enter the collision zone, which is depicted in the lower left part, where the OH packet out of the Stark decelerator cross the H_2 packet from the Even-Lavie valve, which is mounted on top of a helium cryostat. Scattered products were probed with the laser beam intersecting the collision zone (lower blue arrow).

II. METHOD

A. Experiment

1. Experimental setup

The experiments were carried out in a crossed-beam scattering apparatus schematically depicted in Fig. 1. The apparatus included the same Stark decelerator[11] used in previous collision experiments to produce velocity-controlled packets of OH($X^2\Pi$) radicals in the $j = 3/2\ F_1 f$ level.[10,29–31]

Hydroxyl (OH) was prepared by ArF excimer laser (193 nm) photodissociation of nitric acid seeded in a carrier gas and expanded from a pulsed valve (General Valve, Series 99) on which a short quartz capillary was mounted around the orifice. Most of the OH radicals in the supersonic beam were in the lowest OH rovibronic level ($X^2\Pi$, v = 0, $j = 3/2$). The OH(X) rotational levels are split into two so called Λ-doublets denoted[32] e and f of opposite spectroscopic parity ($\epsilon = +1$ and -1, respectively). The spectroscopic parity ϵ is related to the parity p under inversion by $p = \epsilon(-1)^{j-1/2}$. The energetic splitting of the Λ-doublets in the lowest rotational level is only 0.056 cm^{-1}, so that both Λ-doublet levels had approximately equal populations in the supersonic beam.

The OH beam passed through a skimmer into a differentially pumped chamber, where a 3 cm long hexapole collimated the beam into the 2.6 m long Stark decelerator consisting of 317 electrode pairs. OH molecules in the low-field seeking quantum state ($j = 3/2\ F_1 f$) were decelerated and guided, or accelerated, by applying high-voltage switching schemes using the so-called $s = 3$ mode of operation.[11,33] After leaving the Stark decelerator, the OH packet entered the scattering/detection chamber through an aperture which shielded the detection zone not only from residual electric fields of the Stark decelerator but also provided a differential pumping stage. More than 98% of the OH molecules leaving the Stark decelerator reside in the $j = 3/2\ F_1 f$ level.[29]

The H_2 target beam was produced with a commercial Even-Lavie valve,[34] mounted on top of a helium-cryostat. The

OH packet overlapped with the target H_2 beam 61 mm behind the last stage of the decelerator. The two beams crossed at an angle of 45°.

The temperature of the Even-Lavie valve could be actively stabilized at any temperature between 10 and 300 K. Since the boiling point of H_2 is about 20 K, the valve was never cooled down below 40 K in order to avoid clustering in the beam or mechanical clogging of the nozzle. Within this temperature range, H_2 velocities between 950 and 2500 m/s are accessible. A 50 mm long conical skimmer of 3 mm diameter was mounted 150 mm beyond the orifice, where the H_2 molecules entered the differentially pumped scattering/detection chamber. The intersection volume of the two beams was 300 mm farther downstream of the skimmer. In order to collimate the target beam in the transverse direction, a slit of adjustable width (widths 5, 4, 3, 2, 1, and 0.5 mm) was installed 60 mm in front of the interaction volume.

A fast ion gauge (B-451 Fast Ion Gage Tube, Jordan TOF Products, Inc.) was used to characterize the H_2 beam properties, such as arrival time and pulse duration, from time of flight (TOF) measurements. The gauge was mounted on a translation stage; this enabled measurements with the same detector at various positions downstream of the collimation slit. A caliper ruler allows the exact re-positioning of the fast ion gauge. Throughout the experiment the same two positions were used to perform TOF measurements: one at the intersection point and one 900 mm farther downstream.

The OH radicals were state-selectively detected via laser-induced fluorescence in the $A - X$ (1,0) band near 282 nm. The laser beam intersected horizontally at a 45° angle with the OH beam and 90° with the H_2 beam. The resulting fluorescence in the $A - X$ (1,1) band near 314 nm was collected vertically at 90° by a lens-photomultiplier tube (PMT) combination. The diameter of the laser beam was 9 mm, defining a detection volume much larger than the intersection volume of the molecular packets. Special care was taken to ensure that the whole OH packet was illuminated and that detection was performed in the so-called flux mode. The laser pulse energy was sufficiently high (typically 2.8 mJ) to allow measurement under saturation conditions. Stray light, mainly resulting from the laser radiation, was effectively reduced by light baffles and optical filtering in front of the PMT.

2. Characterization of the H_2 beam

Two different secondary beams were employed, namely, a beam of normal-H_2 (denoted hereafter as n-H_2), consisting of 75% *ortho*-H_2 and 25% *para*-H_2, or a beam of *para*-converted H_2 (hereafter denoted as pc-H_2). Separate spectroscopic experiments were carried out to measure the rotational state distribution in the H_2 beams and to determine the purity of the *para*-converted beam. The latter was prepared in a separate device through the use of a paramagnetic catalyst at low temperature.

(3 + 1) REMPI[35] near 289.5 nm was employed to detect individual H_2 rotational levels. Figure S1 of the supplementary material[36] displays typical REMPI spectra. Only the lowest rotational level of each nuclear spin modification, i.e., $j = 0$ and 1 for *para*-H_2 and *ortho*-H_2, respectively, was found to be populated in the supersonic beams. The pc-H_2 beam was found to contain less than 2% *ortho*-H_2.

3. Experimental procedures and data analysis

Variation in the velocity of either one of the reagent beams resulted in a change of the relative velocity, which allowed scanning of the collision energy. Changing the temperature of the Even-Lavie valve produced H_2 beam velocities that allowed a large variation of the collision energy. The Stark decelerator provided accurate control of the velocity of the OH packets, resulting in a finer variation of the collision energy.

A single high-voltage burst applied to the Stark decelerator to manipulate the final velocity of OH radicals consisted of an acceleration with phase-angle $-\phi$ followed by a deceleration with phase angle ϕ.[37] The velocity of the OH packets was varied by switching unequal durations of acceleration and deceleration within the same burst. The produced OH packets had the same spatial dimensions independent of their final velocity, thus making the analysis that depends on the spatial overlap of the two molecular packets less prone to systematic errors.

Section III B 2 shows measurements of (relative) cross sections in the collision energy range 70–150 cm^{-1}, where the OH beam was generated by seeding the nitric acid precursor in krypton. The supersonic beam, with a mean velocity of 495 m/s, was injected into the Stark decelerator, with which the velocity was tuned between 170 m/s and 690 m/s. The H_2 velocity was set to 1320 or 1530 m/s, produced with valve temperatures of 82 K and 107 K, respectively, which yielded collision energy ranges of 70–110 cm^{-1} and 100–150 cm^{-1}.

For measurement at a higher collision-energy resolution, described in Sec. III B 3, a H_2 beam of velocity 1151 m/s was produced with a valve temperature of 65 K while the OH packets were tuned between 1410 m/s and 1643 m/s using a mixture of helium and neon as the seed gas for the OH beam. In this series of runs, only the $j = 3/2\ F_1 f \rightarrow j = 5/2\ F_1 e$ transition was investigated.

The fluorescence signals for each final level were corrected for the differing fluorescence excitation rates since different optical transitions, which have differing excitation rates, were employed for detection of the various rotational levels. These excitation rates are listed, for instance, in Ref. 29. These collision-induced signals were normalized with the intensity of the incoming beam at each collision energy and then divided by the product of the relative velocity and the three-dimensional spatial overlap volume of the two molecular packets, integrated over time up to the moment of detection.

Since the densities of the two packets were not quantitatively determined, we could not extract absolute cross sections. Instead, we determined relative cross sections by dividing the corrected collision-induced signals by the sum of the corrected signals for all inelastic channels. In Sec. III B 2, we report the relative cross sections as percentages of the total inelastic cross section at a given collision energy.

The Stark decelerator was operated at a repetition rate of 10 Hz while the H_2 packets were produced at 5 Hz. This allowed determination of the collision-induced signals from the difference of the fluorescence signals resulting from

alternating shots in the experiment. To eliminate the influence of long-term drifts in the experiment, the collision energy was varied in a quasi-continuous cycle. To this end, the Stark decelerator is programmed to modify the OH velocities from the lowest to the highest and in reverse on every third shot of the experiment. For each collision energy, an arithmetic mean was computed from the collision-induced signals in all repetitions of the experiment. A confidence interval was estimated from the standard error of the mean $\Delta = d/\sqrt{n}$, where d and n are the standard deviation and the number of repetitions, respectively.

B. Scattering calculations

The theory of scattering between a molecule in a $^2\Pi$ electronic state and a diatomic molecule in a $^1\Sigma^+$ state has been described previously[18,19,38] (see also the supplementary material with Ref. 24). The PES's employed in the determination of the cross sections are taken from Ref. 24. As noted in the Introduction, we computed PES's from fits to *ab initio* points obtained with both MRCISD+Q(Davidson) and RCCSD(T)-F12a calculations [denoted below as MRCI and CCSD(T), respectively]. We compare cross sections computed with both of these fits but use the latter method predominantly. Close-coupling calculations were performed both with the HIBRIDON suite of programs,[39] recently modified to support $^2\Pi$–$^1\Sigma^+$ collisions, and, totally independently, with a scattering program developed in Nijmegen.[38] Care was taken to compare the results of the two scattering programs and the convergence of the cross sections.

In all the calculations, the rotational constant B (59.322 and 29.9043 cm^{-1}, respectively, for H_2 and D_2) was taken from Ref. 40. The spin-orbit constant A and the Λ-doubling parameters p and q for the v = 0 level of OH were taken from Ref. 41. Depending upon the collision energy, we included OH rotational levels up to j = 6.5 in our close-coupling basis at the higher collision energies. The highest H_2/D_2 rotational levels included considering the scattering with j = 0–3 H_2/D_2 were, respectively, 2, 3, 4 (6 for higher collision energies), and 5. Partial waves up to $J \leq 30.5$–$89.5\hbar$, depending upon collision energy, were included in the calculations. The convergence of the integral cross sections upon the close-coupling basis set was carefully checked. We denote hereafter the rotational angular momenta of OH and H_2/D_2 as j_1 and j_2, respectively.

III. RESULTS

A. OH–H_2 collisions: Calculations and comparison with older work

We first consider OH–H_2 collisions up to a total energy of 500 cm^{-1} and compare our computed cross sections with those from previous scattering calculations by Offer *et al.*[19,22] that employed the OvH PES's.[22] At higher collision energy, the scattering dynamics should be sensitive primarily to the repulsive wall of the potential, which has not been significantly tested in our previous bound-state calculations.[24]

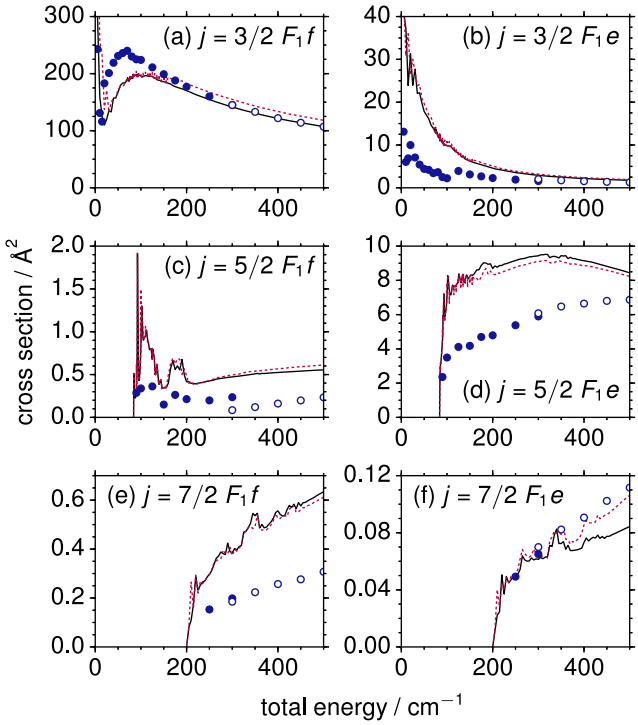

FIG. 2. State-to-state integral cross sections as a function of total energy for OH ($j_1 = 3/2$ F_1f to several low-lying F_1 levels) in collisions with *para*-H_2 ($j_2 = 0 \rightarrow 0$). The solid and the dashed lines represent cross sections computed using the CCSD(T) and the MRCI PES's, respectively. The cross sections from calculations by Offer *et al.* (taken from Ref. 19) are plotted in dots (close-coupling calculations) or circles (coupled-states calculations).

We present in Figs. 2 and 3 computed energy-dependent OH–*para*-H_2 cross sections out of the $j_1 = 3/2$ F_1f level. Cross sections computed using the OvH PES's[22] (taken from the supplementary material of Ref. 19 and computed excitation cross sections from de-excitation cross sections using detailed balance) are also plotted for comparison. For a proper

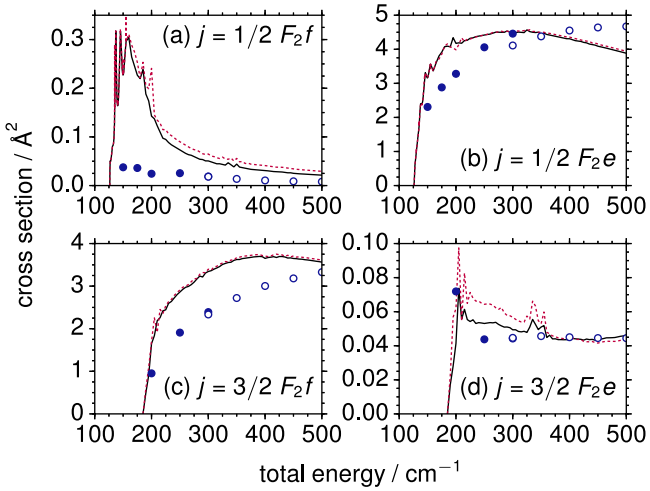

FIG. 3. State-to-state integral cross sections as a function of total energy for OH ($j_1 = 3/2$ F_1f to several low-lying F_2 levels) in collisions with *para*-H_2 ($j_2 = 0 \rightarrow 0$). The solid and the dashed lines represent cross sections computed using the CCSD(T) and the MRCI PES's, respectively. The cross sections from calculations by Offer *et al.* (taken from Ref. 19) are plotted in dots (close-coupling calculations) or circles (coupled-states calculations).

comparison with the OvH calculations, we considered only the j_2-preserving transitions ($j_2 = 0 \rightarrow 0$) in our calculations, and the total energy is the OH rotational energy relative to the $j_1 = 3/2$ F_1e level plus the collision energy. Cross sections for other transitions are available in the accompanying EPAPS document.[36]

In general, the cross sections computed with the CCSD(T) and the MRCI PES's agree very well. For all transitions, our results are similar in magnitude to the cross sections computed by Offer *et al.* The most significant differences, however, appear in the inelastic transitions with the largest cross sections, namely, $j_1 = 3/2$ $F_1f \rightarrow j_1 = 3/2$ F_1e and $j_1 = 3/2$ $F_1f \rightarrow j_1 = 5/2$ F_1e. As will be discussed in Sec. III B, these are transitions most sensitive to the accuracy of the PES's.

In Figs. 4 and 5, we present energy-dependent cross sections when the collision partner of OH is *ortho*-H_2 ($j_2 = 1 \rightarrow 1$). The agreement between the cross sections computed with our PES's and the OvH PES's is significantly better when the collision partner of OH is *ortho*-H_2. This is also the case when comparing the cross sections computed from the OvH and the KF PES's, where the cross section for the $j_1 = 3/2$ $F_1f \rightarrow j_1 = 3/2$ F_1e transition differs by a factor of ~5 (Table II of Ref. 19). As we will discuss later, the OH–*para*-H_2 collision dynamics is dominated by the dispersion interactions rather than the multipole-multipole electrostatic interactions and hence requires more sophisticated electronic structure theory to describe properly.

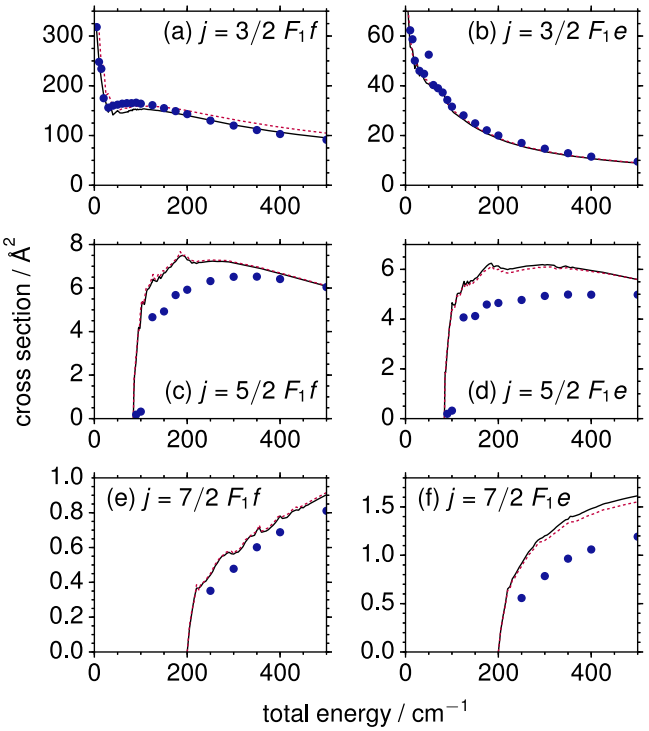

FIG. 4. State-to-state integral cross sections as a function of total energy for OH ($j_1 = 3/2$ F_1f to several low-lying F_1 levels) in collisions with *ortho*-H_2 ($j_2 = 1 \rightarrow 1$). The solid and the dashed lines represent cross sections computed using the CCSD(T) and the MRCI PES's, respectively. The cross sections from an earlier close-coupling calculation (taken from Ref. 19) are plotted in dots.

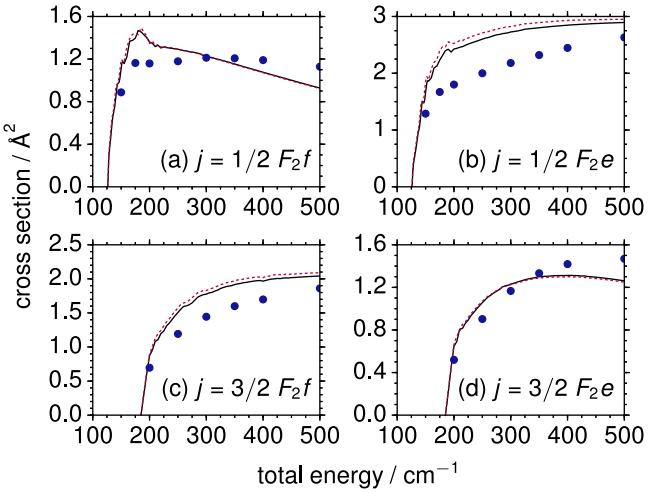

FIG. 5. State-to-state integral cross sections as a function of total energy for OH ($j_1 = 3/2$ F_1f to several low-lying F_2 levels) in collisions with *ortho*-H_2 ($j_2 = 1 \rightarrow 1$). The solid and the dashed lines represent cross sections computed using the CCSD(T) and the MRCI PES's, respectively. The cross sections from an earlier close-coupling calculation (taken from Ref. 19) are plotted in dots.

We also show in Sec. II of the supplementary material[36] our relative cross sections at a collision energy of 595 cm^{-1} in comparison with OvH calculations[19] and the experimental results of Schreel and ter Meulen.[9] While all the results are in reasonable agreement, our calculations, based on a higher level of electronic structure theory and treatment of dynamics, do not result in better agreement with the experiment. However, no hard conclusions can be drawn from this experiment–theory comparison since only one collision energy is considered. As Figs. 2–5 and S3–S5 of the supplementary material[36] illustrate, comparison of absolute cross sections between scattering calculations employing different potentials is a much more sensitive test of the quality of a potential than comparison of relative cross sections. While molecular beam experiments can provide considerable information on the collision dynamics, only relative cross sections are usually measured in such experiments.

B. OH–H_2 collisions: Comparison of theory with new experimental data

1. *Absolute cross sections*

Elastic and inelastic state-to-state integral cross sections for collisions of OH with *para*- or *ortho*-H_2 in the energy range 75–150 cm^{-1} were computed through close-coupling calculations with the inclusion of all rotational levels with $j_1 \leq 19/2$ of OH and with $j_2 \leq 3$ of H_2. In the corresponding experiments (discussed above), OH was prepared in its $j_1 = 3/2$ F_1f state by the Stark decelerator that was used to tune its velocity, so calculations are reported for just this initial level. Calculations were carried out for the lowest rotational level of each nuclear spin modification of H_2 ($j_2 = 0$ and 1 for *para*- and *ortho*-H_2, respectively) since excited rotational levels had negligible population in the secondary beams (see Sec. II A 2).

Integral inelastic cross sections for collision of OH($X^2\Pi$, $j_1 = 3/2$ F_1f) with *para*-H_2 and *ortho*-H_2 collisions are shown

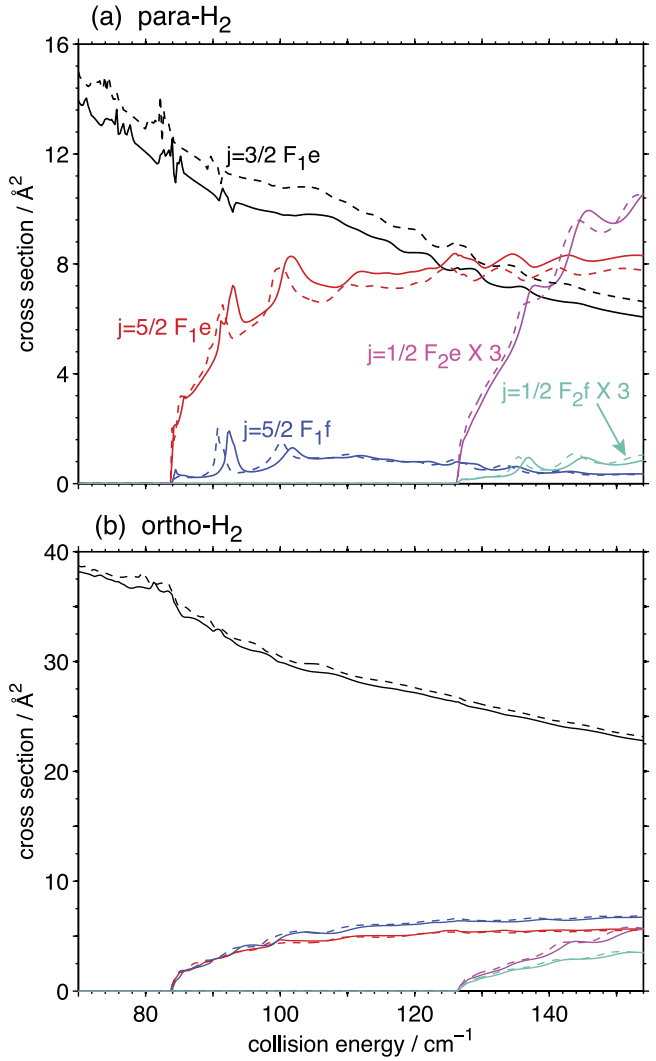

FIG. 6. Integral inelastic cross sections for collisions between OH($X^2\Pi, j_1 = 3/2\ F_1 f$) with (a) *para*-H_2 ($j_2 = 0$) and (b) *ortho*-H_2 ($j_2 = 1$) *vs.* collision energy over the range 75–150 cm^{-1}. Note the different scalings of the vertical axes. The cross sections were computed with the CCSD(T) (solid lines) and MRCI (dashed lines) PES's. Cross sections for transitions to the $j_1' = 1/2\ F_2 e/f$ levels have been multiplied by a factor of 3 for clarity.

in Fig. 6. While the cross sections of a given transition computed with the two PES's have very similar magnitudes and energy dependences, we do see some differences. In particular, the positions of both the sharp and broad resonances are shifted slightly. In previous work,[24] we showed that the CCSD(T) and MRCI PES's were quite similar. In particular, the computed dissociation energies D_0 of the OH–*ortho*-H_2 and OH–*para*-H_2 complexes differed by only 2 cm^{-1}. The slight differences in the resonance energies are an indication of the sensitivity of these features to the details of the PES's.

We note some striking differences when comparing the cross sections in the two panels in Fig. 6. First, the j_1-conserving, but parity-changing, transition to the $j_1' = 3/2\ F_1 e$ level of OH has a much larger cross section for collisions with H_2 $j_2 = 1$ than for collisions of H_2 $j_2 = 0$. Second, the cross sections for the transitions to OH levels with the same final j_1 but different parity are almost equal for *ortho*-H_2 while the probabilities of such transitions differ strongly for *p*-H_2. In the latter case, transitions that conserve the parity p, such as transitions to the $j_1' = 5/2\ F_1 e$ and $j_1' = 1/2\ F_2 e$ levels, are much more probable than transitions to the same final j_1 level that involve a change of parity. In particular, we see that for *para*-H_2 at higher collision energies, the parity-conserving $j_1 = 3/2\ F_1 f \rightarrow j_1' = 5/2\ F_1 e$ transition becomes even more probable than the j-conserving but parity-changing transition to the $j_1' = 3/2\ F_1 e$ level. A similar clear propensity for parity-conserving transitions is observed in collisions of OH with rare gas targets, especially in collisions of OH with He.[30]

The reason for these differences is that the dominant mechanism in the parity-changing OH–H_2 collisions involves the (first-order electrostatic) interaction of the OH dipole moment with the quadrupole and hexadecapole moments of H_2.[42] However, the lowest level of *para*-H_2, with $j_2 = 0$, behaves as a spherical, structureless particle, and its multipole moments average out to zero in first order. They become effective only in second order by some admixture of $j_2 = 2$, which is higher in energy by about 360 cm^{-1}. For *ortho*-H_2 $j_2 = 1$, on the other hand, there are strongly anisotropic first-order dipole-quadrupole and dipole-hexadecapole interactions.

2. Relative cross sections

Figure 7 displays the measured relative cross sections for collisions of Stark decelerated OH($j_1 = 3/2\ F_1 f$) with *n*-H_2 and *pc*-H_2, as a function of the collision energy over 70–150 cm^{-1}. All energetically accessible final levels were observed, and the energy thresholds for both fine-structure conserving and fine-structure changing transitions are clearly seen.

The most direct comparison between experiment and theory can be made by looking at the state-to-state relative cross sections for collisions of OH with *para*-H_2 ($j_2 = 0$) and *ortho*-H_2 ($j_2 = 1$). These can be determined from the measured signals plotted in Fig. 7 since the population ratios of $j_2 = 0$ and 1 were determined, as described in Sec. II A 2 and the supplementary material.[36] There is strong evidence that the number density in the H_2 beam does not change appreciably when the gas supply is exchanged between *n*-H_2 and *pc*-H_2. The valve settings (temperature, stagnation pressure, and valve-opening time) were kept the same. As described in the supplementary material,[36] the signal intensity and time-of-flight profile as measured with the fast ion gauge did not show significant differences between the two gases.

Figure 8 presents the experimentally derived relative cross sections for collisions of OH($X^2\Pi, j_1 = 3/2\ F_1 f$) with *para*-H_2 ($j_2 = 0$) and *ortho*-H_2 ($j_2 = 1$). The confidence intervals have not been plotted in this figure for clarity but are similar to those shown in Fig. 7. Also plotted in Fig. 8 for comparison are the relative cross sections computed using the CCSD(T) PES's. These have been convoluted with the experimental collision energy spread (taken as a Gaussian with FWHM ≈ 17 cm^{-1}). Comparing the computed cross sections in Fig. 6 with those plotted in Fig. 8, we see that the width in collision energy has blurred out the resonance features in the computed cross sections.

The agreement between experiment and theory is good for both sets of cross sections. The dramatic differences in

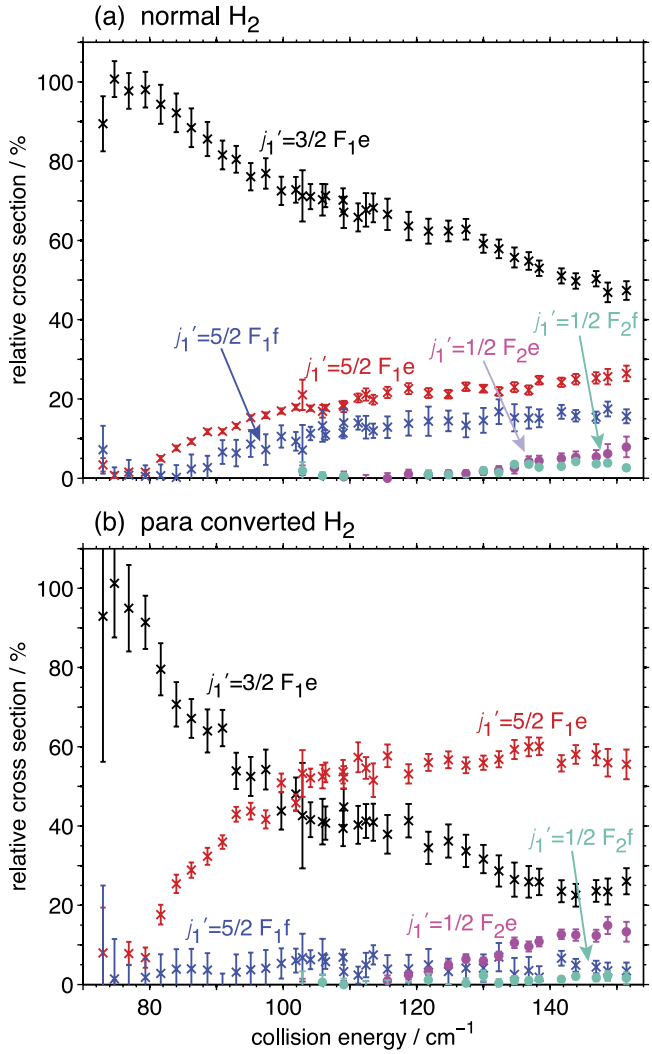

FIG. 7. Measured relative cross sections for collisions of OH($X^2\Pi, j_1 = 3/2\ F_1 f$) with (a) *n*-H_2 and (b) *pc*-H_2 ($j_2 = 0$) as a function of the collision energy over the range 75–150 cm^{-1}.

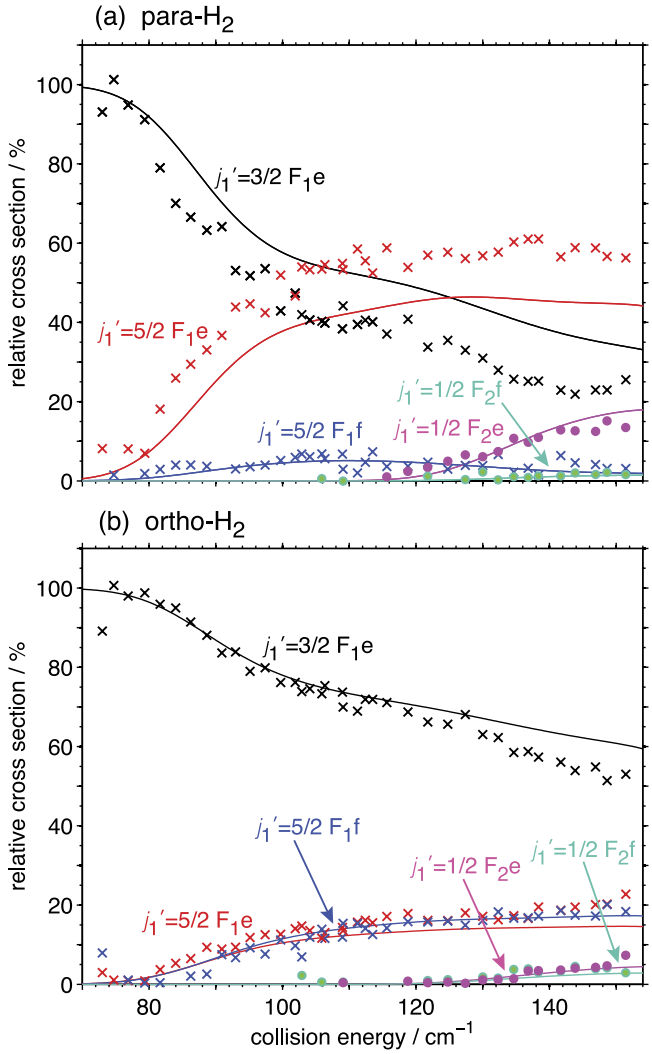

FIG. 8. Experimental (symbols) and theoretical (solid lines) relative cross sections for collisions of OH($X^2\Pi, j_1 = 3/2\ F_1 f$) with (a) *para*-H_2 ($j_2 = 0$) and (b) *ortho*-H_2 ($j_2 = 1$).

the magnitudes of the state-to-state cross sections for H_2 in the $j_2 = 0$ and 1 initial rotational levels seen in Fig. 6 are also apparent in the experimentally determined relative cross sections plotted in Fig. 8. The most significant difference between the experimental and computed relative cross sections is for the transitions to the $j_1' = 3/2\ F_1 e$ and $j_1' = 5/2\ F_1 e$ levels for collisions with *para*-H_2 $j_2 = 0$. The theoretical relative cross section for the transition to the $j_1' = 3/2\ F_1 e$ level is computed to be larger than the corresponding measured value, while the relative cross section for the transition to the $j_1' = 5/2\ F_1 e$ level is underestimated by theory.

These differences in the magnitudes of the cross sections could be due to inadequacies in the PES's used in the computation of the cross sections. In our work on the calculation of the OH–H_2 PES's,[24] we carried out additional calculations on the interaction energy at several nuclear geometries, beyond full MRCI and RCCSD(T) calculations of the PES's. The explicitly correlated CCSD(T)-F12a calculations and canonical CCSD(T) calculations with complete basis set (CBS) extrapolation gave similar results. Calculations with full triples (CCSDT)[43] gave results similar to those with perturbative inclusion of triples. Our MRCI and RCCSD(T) PES's were computed with the OH and H_2 bond distances fixed at r_0. Vibrational averaging over r(OH) led to a slight increase in the repulsive interaction, while vibrational averaging over $r(H_2)$ had little effect at the selective geometries investigated. Our present computational resources are not sufficient to carry out CCSDT calculations (full triples), or vibrationally averaged calculations, for the ≥6000 points used for the determination of the CCSD(T) PES's.

In our measurements, the *n*-H_2 and *pc*-H_2 beams were found to have the same intensities when the gases were exchanged. In addition to the relative cross sections, we can also compare the signals strengths for detection of a given final level with the two target beams in order to gauge the ratio of the absolute cross sections for collision of $j_2 = 0$ and 1. Figure S2 of the supplementary material[36] presents comparison between measured and computed ratios of the absolute cross sections for collision of OH with *para*-H_2 and *ortho*-H_2 as a function of the collision energy for each of the final levels. These measured ratios reproduce well (within large error bars) the calculated ratios of the cross sections.

3. Investigations with high collision energy resolution

The calculated cross section for the OH $j_1 = 3/2\ F_1 f \rightarrow j_1' = 5/2\ F_1 e$ transition in collision with *para*-H_2 $j_2 = 0$, plotted in Fig. 6(a), shows resonance features for collision energies near 93 and 102 cm^{-1}. Similar resonance features were found in calculated cross sections for the collision of OH with He and Ne and were analyzed in detail.[26] In order to investigate resonances in OH–H_2 collisions, the OH $j_1 = 3/2\ F_1 f \rightarrow j_1' = 5/2\ F_1 e$ transition in collision with H_2 $j_2 = 0$ was measured with higher collision energy resolution. This was accomplished by using a kinematically more favorable collision geometry.[44] The relevant settings of the OH velocities and the *pc*-H_2 velocity are given in Sec. II A. The transverse velocity distribution of the *pc*-H_2 beam was identified as the factor limiting the collision energy resolution. It was therefore reduced with a 2 mm wide slit, shown in Fig. 1.

The black data points in Fig. 9 show the experimentally determined excitation function for the OH $j_1 = 3/2\ F_1 f \rightarrow j_1' = 5/2\ F_1 e$ transition in collision with *pc*-H_2 ($j_2 = 0$) as a function of the collision energy between 78 and 103 cm^{-1}. The experimental collision energy distribution (FWHM ≈ 2.3 cm^{-1}) was estimated using the kinematic model described in the supplementary material.[36] The red dashed and solid lines in Fig. 9 display, respectively, the theoretical cross section and the same quantity convoluted with the experimental collision energy resolution. Both theoretical cross sections are scaled by an identical constant factor to compare them with the experimental data. The overall agreement is good. In particular, the steep increase of the cross section at the rotational threshold, as well as its dependence on the collision energy, is reproduced almost within the experimental confidence interval. The increase in the experimental excitation function at threshold is faster than predicted by the convoluted theoretical calculation. This suggests that the collision energy resolution in the experiment is probably better than the estimated 2.3 cm^{-1} (FWHM).

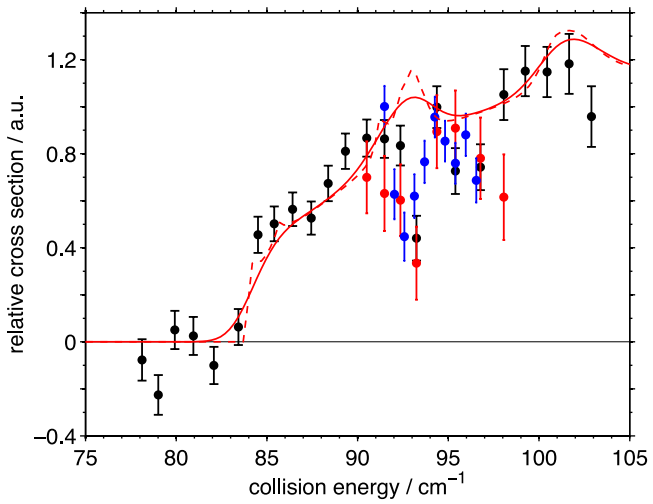

FIG. 9. The black points display the experimentally determined excitation function for the OH $j_1 = 3/2\ F_1 f \rightarrow j_1 = 5/2\ F_1 e$ transition in collision with *pc*-H_2 ($j_2 = 0$) as a function of the collision energy between 78 and 103 cm^{-1}. Two additional sets of measurements (red and blue points) were conducted under different conditions and sampled the 90–97 cm^{-1} collision energy range in more detail. The red dashed and solid lines show the pure theoretical cross section and this cross section convoluted with the experimental collision energy resolution (FWHM ≤ 2.3 cm^{-1}), respectively.

The most striking feature in Fig. 9 is the difference between the experimental and theoretical cross sections around 93 cm^{-1}, where a dip in the cross section of ca. 50% is found in the measurements relative to adjacent data points. In the same collision energy range, the theoretical cross section increases slightly due to a shape resonance. To confirm the measurements, the experiment was repeated under different conditions while sampling the collision energy range between 90 and 97 cm^{-1} in greater detail. The OH packets are produced prior to collision using different high-voltage switching schemes of the Stark decelerator, as well as different rare gas mixtures for the initial OH beam. The results are depicted in the red and blue points in Fig. 9. All the sets of experimental data agree to within the plotted confidence intervals.

A possible explanation for the dramatic difference in the energy dependences of the measured and computed OH $j_1 = 3/2\ F_1 f \rightarrow j_1' = 5/2\ F_1 e$ excitation functions is that positions of the resonance as predicted by the theoretical scattering calculations are inaccurate due to small inaccuracies in the PES's. We see in Fig. 6(a) that the predicted resonance energies are slightly different when the cross sections are computed using the CCSD(T) and MRCI PES's. However, for neither set of PES's is a large dip found in the computed excitation functions.

We considered several explanations for the observed dip in the excitation function near 93 cm^{-1}. At a resonance the lifetime of the collision complex will be longer than for collisions at nearby energies. This lifetime can be estimated from the energy derivative of the *S*-matrix.[26] We obtained a lifetime of about 50 ps for the computed resonance near 93 cm^{-1}, which is indeed longer than what we would expect for a collision of OH with H_2 (we estimate $\tau_{col} \simeq 1$ ps). If a chemical reaction were to occur within this lifetime, then the signal for the $j_1' = 5/2\ F_1 e$ level would be reduced. This seems highly improbable since the barrier for the OH + H_2 reaction is $\approx$2130 cm^{-1} (Refs. 20, 45, and 46) which is much larger than the collision energy. We can similarly eliminate the possibility that a secondary collision could dissociate the transient OH–H_2 complex and lead to a significant dip in the excitation function since the probability of a secondary collision of the complex with background gas is estimated to be $\approx 10^{-5}$.

The angular distribution of the scattered OH could be different for a collision at an energy near that of a resonance.[26] In the present experiment, we are detecting the heavy collision partner at an energetic threshold, so that the OH center-of-mass velocity is much smaller than the velocity of the center of mass of the complex. Hence, the presence of the resonance should not significantly affect the laboratory angular distribution. Polarization effects were also considered since the detection laser was linearly polarized in the scattering plane. Collision-induced alignment was quantified by computing $|m_j|$-resolved DCS's for the $j_1' = 5/2\ F_1 e$ final level. No substantial changes at the resonance energy were found in either the degeneracy-averaged DCS, or the DCS for specific OH $|m_j|$ sublevels.

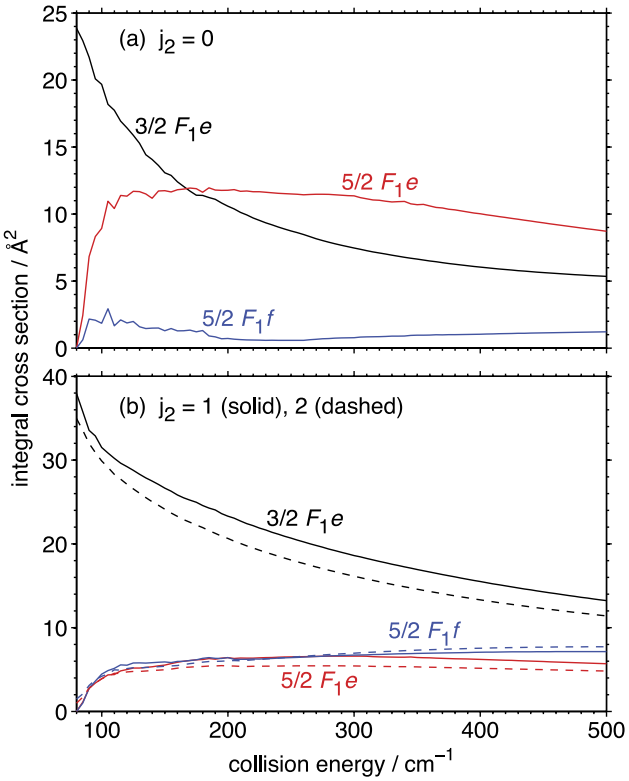

FIG. 10. Computed state-to-state integral cross sections as a function of the collision energy for transitions out of the OH $j_1 = 3/2$ F_1f initial level to other F_1 levels in collisions with D_2. The final levels for each transition are indicated. Panel (a) presents cross sections for the D_2 $j_2 = 0$ initial rotational level, while panel (b) applies to the D_2 $j_2 = 1$ and 2 initial rotational levels. The plotted cross sections represent sums over all accessible final D_2 rotational levels.

A final possibility would be the occurrence of nuclear spin conversion from *para*-H_2 ($j_2 = 0$) into *ortho*-H_2 ($j_2 = 1$). In principle, this could be caused during the lifetime of the collision complex by the difference in the magnetic field of the paramagnetic OH radical at the sites of the H_2 protons. Energetically it would be possible: the energy required to convert H_2 $j = 0$ into $j = 1$ is 118.6 cm^{-1}, and the collision energy is ≈93 cm^{-1}. This seems insufficient, but one must also consider that the binding energies D_0 of the OH–pH_2 and OH–oH_2 complexes are 36 and 54 cm^{-1}, respectively.[24,25] This would imply that the complex must remain bound after the conversion, which would lead to a loss of the detected $j_1' = 5/2$ F_1e signal. We estimated the conversion probability from the size of the coupling between the magnetic moments of the paramagnetic OH species and the H_2 proton spins, but we found that it is far too small to account for the dip in the measured signal.

Thus, we are as yet unable to offer a cogent physical explanation of the observed dip in the measured OH $j_1 = 3/2$ $F_1f \rightarrow j_1' = 5/2$ F_1e excitation function as the collision energy approaches 93 cm^{-1}. Mysteriously, at the same energy, theory predicts a slight increase due to a shape resonance.

C. OH–D_2 collisions

In this section, we consider collisions between OH and D_2 and compare our calculations with the measurements of Kirste *et al.*[10] These experiments probed a higher range of collision energies than the OH–H_2 experiments described in Sec. III B. Again, we consider the OH $j_1 = 3/2$ F_1f initial level since in both experiments, a similar Stark decelerator was used. All calculations reported in this section employed the CCSD(T) PES's.

In Figs. 10 and 11, we present computed integral cross sections for transitions out of the OH $j_1 = 3/2$ F_1f initial level in collisions with the D_2 $j_2 = 0$, 1, and 2 initial rotational levels. Figure 10 displays state-to-state integral cross sections for fine-structure conserving transitions, while Fig. 11 displays cross sections for fine-structure changing transitions. As is the case of OH–H_2 collisions, the transition from the upper to the lower $j_1 = 3/2$ F_1 Λ-doublet dominates at low energies, while the transition to the $j_1' = 5/2$ F_1 level becomes significant at higher collision energies above its energetic threshold. Comparing panels (a) and (b) of Fig. 10, we see that the cross sections for collisions involving the D_2 $j_2 \geq 1$ initial levels are significantly larger than for $j_2 = 0$.

Since the quadrupole moment in D_2 $j_2 = 0$ averages to zero, the long-range dipole-quadrupole anisotropy will contribute only for inelastic collisions involving D_2 in $j_2 > 0$. Since this anisotropy does contribute both for $j_2 = 1$ and $j_2 = 2$, we see in Fig. 10(b) that the cross sections for the scattering out of these two initial levels are similar in magnitude.

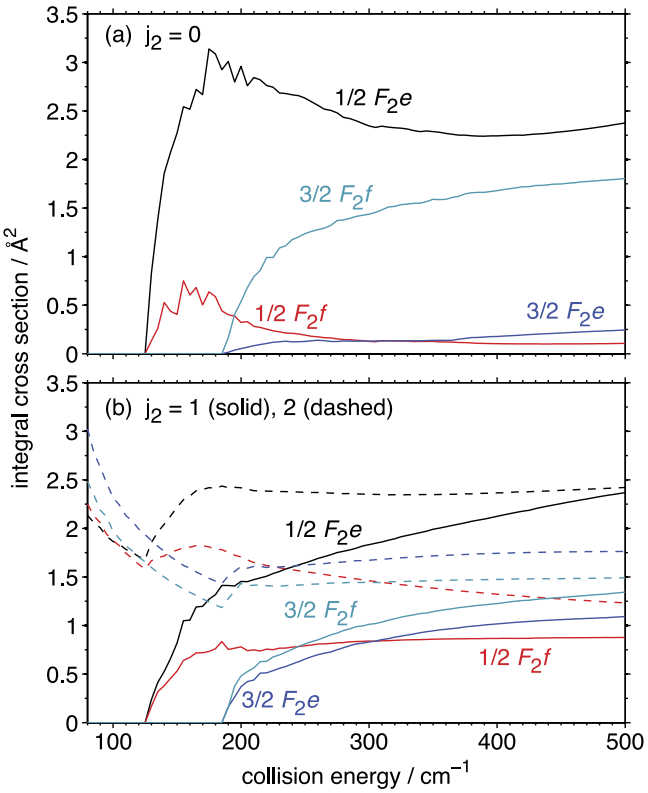

FIG. 11. Computed state-to-state integral cross sections as a function of the collision energy for transitions out of the OH $j_1 = 3/2$ F_1f initial level to F_2 levels in collisions with D_2. The final levels for each transition are indicated. Panel (a) presents cross sections for the D_2 $j_2 = 0$ initial rotational level, while panel (b) applies to the D_2 $j_2 = 1$ and 2 initial rotational levels. The plotted cross sections represent sums over the final D_2 rotational levels.

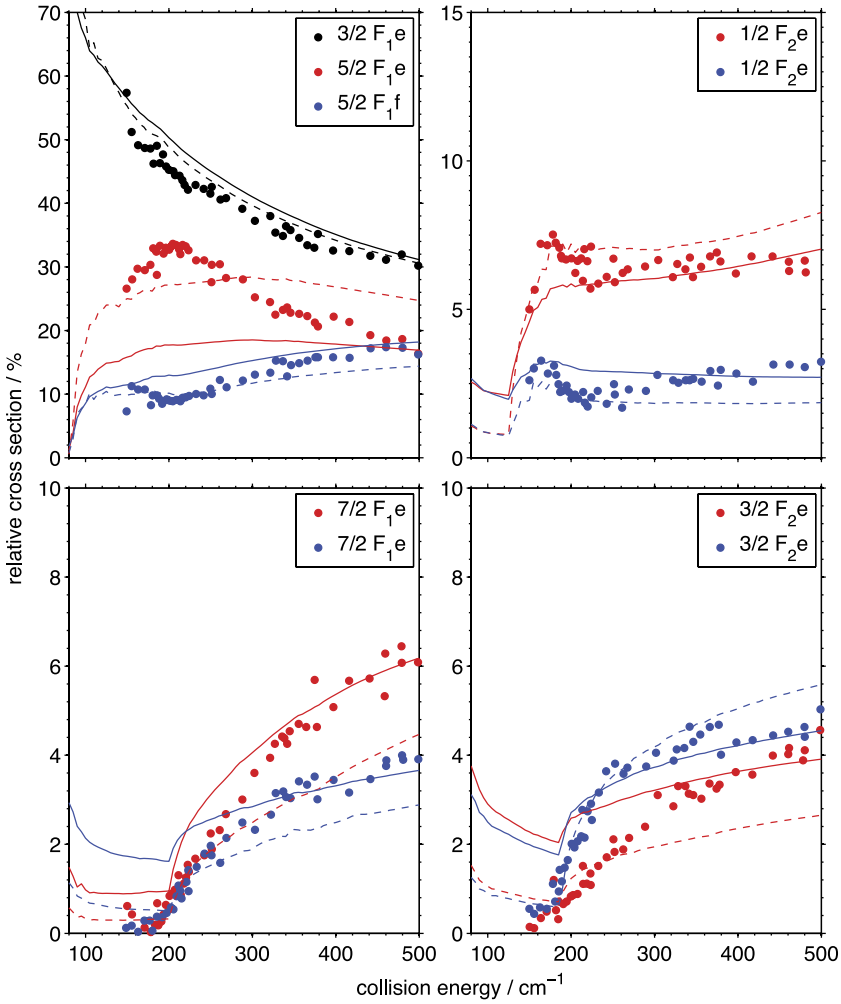

FIG. 12. Experimental and computed relative state-to-state cross sections as a function of the collision energy for transitions out of the OH $j_1 = 3/2$ $F_1 f$ initial level in collisions with D_2. The final levels are denoted in the upper right corner of each panel. The experimental data, taken from Ref. 10, are shown as dots. The theoretical results, shown as lines, were obtained assuming that the D_2 rotational temperature was 93 K (solid lines) and 293 K (dashed lines).

Cross sections for fine-structure changing transitions, displayed in Fig. 11, are smaller than those for fine-structure conserving transitions. We see in Figs. 11(a) and 11(b) that the cross sections rise strongly from their energetic thresholds in collisions with D_2 $j_2 = 0$ and 1. By contrast, the cross sections for the D_2 $j_2 = 2$ initial level are significant below this nominal threshold. This behavior is due to the occurrence of $j_2 = 2 \rightarrow 0$ transitions at lower collision energies. At such collision energies, these cross sections are comparable in magnitude to the cross sections for the corresponding $j_2 = 2 \rightarrow 2$ transitions.

Figure 12 presents a comparison between the experimental measurements of Kirste *et al.*[10] and our computed cross sections *vs.* collision energy for transitions out of the OH $j_1 = 3/2$ $F_1 f$ initial level in collisions with D_2. Kirste *et al.* report their measurements as relative state-to-state cross sections, namely, as a percentage of the total rotationally inelastic cross section at a given collision energy, and we present our calculations similarly. To make a definitive comparison between experiment and theory, it is necessary to know the rotational temperature of the D_2 beam. Unfortunately, this was not measured in the experiment. The authors of Ref. 10 stated that six temperatures ranging from 93 to 293 K were used for the pulsed valve producing the D_2 beam.

We can expect an undetermined, but likely small, degree of rotational cooling in the D_2 supersonic beam expansion. To carry out a comparison between theory and experiment, we computed two sets of relative cross sections, including D_2 initial levels up to $j_2 = 3$. We assumed that D_2 was at thermal equilibrium at 93 and 293 K, indicated with solid and dashed lines, respectively, in Fig. 12. These two sets of theoretical cross sections should give an indication of the variation in the relative cross sections upon the D_2 rotational temperature. It should be noted that the D_2 beam source was operated at different temperatures for different collision energy ranges.

There is generally good agreement between the measured and computed relative cross sections, displayed in Fig. 12. We see for the transition with the largest cross section, namely, $j_1 = 3/2$ $F_1 f \rightarrow j_1' = 3/2$ $F_1 e$, that the computed cross section has only a minor dependence upon the D_2 rotational temperature and agrees well with the experimental measurement. The greatest disagreement between theory and experiment is for the transition with the second largest value, the $j_1 = 3/2$ $F_1 f \rightarrow j_1' = 5/2$ $F_1 e$ transition. This is similar to the situation with OH–H_2 collisions (see Sec. III B 2).

IV. DISCUSSION

It is interesting to compare the scattering of OH by p-H_2 in its ground rotational level ($j_2 = 0$) and the helium atom. Kirste *et al.*[31] compared measured relative cross sections for OH–D_2 and OH–He, which have the same collision reduced mass.

Scharfenberg *et al.*[30] have reported relative cross sections for collisions of OH with all the inert gas atoms, and these were compared with computed relative cross sections. Here, we consider OH–H_2 and OH–He absolute integral cross sections.

As noted in Sec. III B 1, the $H_2(j_2 = 0)$ level behaves as a spherical, structureless particle, in analogy with an inert gas atom. In Ref. 24, we compared the PES's for the interaction of $OH(X^2\Pi)$ with $H_2(j_2 = 0)$, He, and Ne. The anisotropies of the PES's are similar. The OH–H_2 attractive interaction is significantly stronger than for OH–He and is comparable to that for OH–Ne. The one difference between H_2 and the inert gas collision partners is that for H_2, the rotational wave function can include some admixture of $j_2 = 2$, and this can lead to some second-order contribution of the H_2 multipole moments.

In Fig. 13, we compare computed integral state-to-state cross sections for collisions of $OH(j_1 = 3/2\ F_1f)$ with H_2 ($j_2 = 0$) and He in the collision energy range 75–150 cm^{-1}. The latter were calculated with the PES's computed by Gubbels *et al.*[26] For OH–H_2, we present calculations carried out with $j_2 = 0$ only and with $j_2 = 0$ and 2 in the H_2 rotational basis. For comparison with OH–He cross sections, it is appropriate to compare with the former OH–H_2 calculations. It is interesting to note in Fig. 13(a) that inclusion of $j_2 = 2$ in the H_2 rotational basis has only a minor effect on the magnitude and energy dependence of the cross sections for transitions to most final levels. The significant exception is the $j_1 = 3/2$ $F_1f \rightarrow j_1 = 3/2$ F_1e transition, for which the cross section is significantly enhanced by inclusion of $j_2 = 2$.

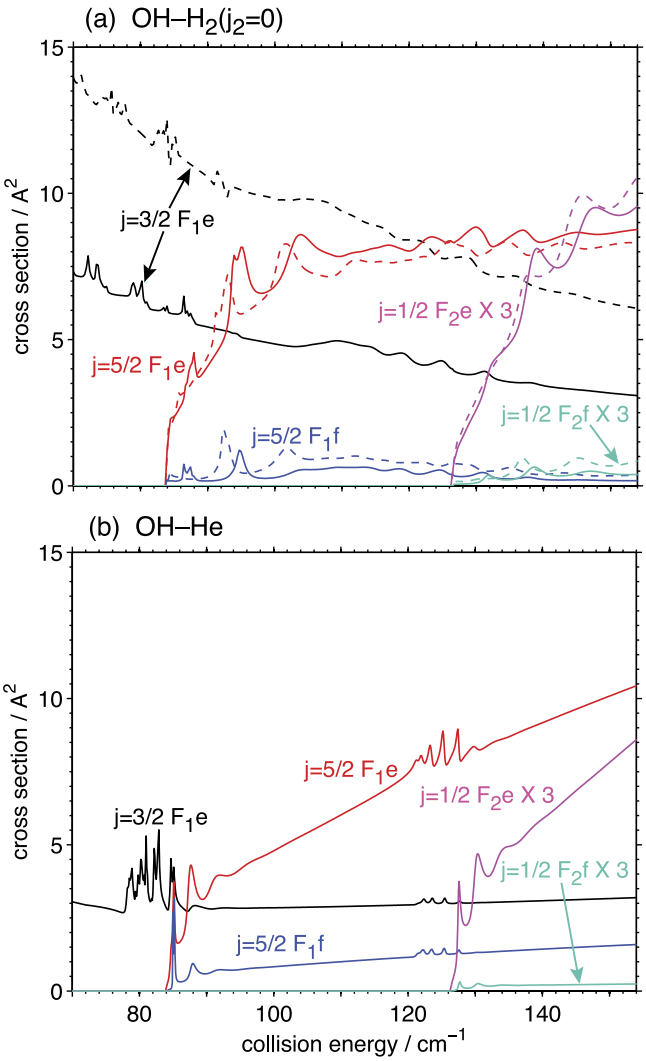

FIG. 13. Integral inelastic state-to-state cross sections for collisions of $OH(X^2\Pi, j_1 = 3/2\ F_1f)$ with (a) $H_2(j_2 = 0)$ and (b) He *vs.* collision energy over the range 75–150 cm^{-1}. The solid and dashed curves in panel (a) denote OH–H_2 calculations that included $j_2 = 0$ only and $j_2 = 0$ and 2, respectively, in the H_2 rotational basis. The cross sections were computed with PES's reported in Refs. 24 and 26, respectively.

We see that the cross section for the parity-changing $j_1 = 3/2$ $F_1f \rightarrow j_1 = 3/2$ F_1e transition is much larger for OH–$H_2(j_2 = 0)$ than for OH–He. For the latter, this transition is enabled by odd-l_1 terms in the angular expansion[47] of the sum $(A' + A'')$ potential, and similar terms for OH–H_2. We see from comparison of Figs. 13(a) and 6(b) that the cross section for this transition is even larger for OH–$H_2(j_2 = 1)$. As noted previously [see Sec. III B 1], the dominant mechanism for this transition involves the electrostatic interaction of the OH dipole moment with the quadrupole moment of H_2.

By contrast, cross sections for the parity-conserving transitions to the $j_1' = 5/2$ F_1e and $j_1' = 1/2$ F_2e levels have similar magnitudes for OH–$H_2(j_2 = 0)$ and OH–He. For both systems, the cross sections to the corresponding parity-changing transitions to the $j_1' = 5/2$ F_1f and $j_1' = 1/2$ F_2f levels are much smaller.

We see from Fig. 13 that for both OH–H_2 and OH–He collisions, as well as for other OH–rare gas collisions,[30] the Λ-doublets of the final rotational levels are not equally populated. Propensity rules for the favored inelastic transitions in collisions of a diatomic molecule in a $^2\Pi$ electronic state with a structureless atom have been derived from a formal analysis of the quantum scattering equations.[48,49] For example, in the Hund's case (a) limit, the cross sections for $\epsilon \rightarrow \epsilon'$ and $-\epsilon \rightarrow -\epsilon'$ transitions should be equal.

Comparison of cross sections for transitions out of the $j_1 = 3/2$ F_1e/f levels plotted in Fig. 14 shows that the above propensity is not at all obeyed in OH–*para*-H_2 ($j_2 = 0$) collisions but is approximately followed for OH–*ortho*-H_2 $j_2 = 1$ collisions. Dagdigian *et al.*[49] have carried out a formal analysis of propensity rules for collisions of $^2\Pi$ molecules with π and π^3 orbital occupancies that approach the Hund's case (b) limit. This analysis has previously been applied to collisions of the OH $j_1 = 3/2$ F_1f level with He.[10] The propensity for parity-conserving transitions was thus rationalized from the importance of even l terms in the angular expansion of the PES. Similarly, we see in Fig. 14(a) that the parity-conserving $j_1 = 3/2$ $F_1f \rightarrow j_1' = 5/2$ F_1e transition in collision with $H_2(j_2 = 0)$ has a large cross section. This propensity is not seen in collisions with $H_2(j_2 = 1)$ because of the presence of $l_2 \neq 0$ terms in the angular expansion of the interaction of OH with H_2 $j_2 \geq 1$ rotational levels.[24]

Interstellar and circumstellar OH masers serve as a very useful probe of physicochemical conditions in astronomical objects that are related to either star formation or late stars. There has been considerable interest in understanding the pump mechanisms that lead to maser emission from excited OH rotational levels.[50–53] Obviously, collision of OH with H_2 is

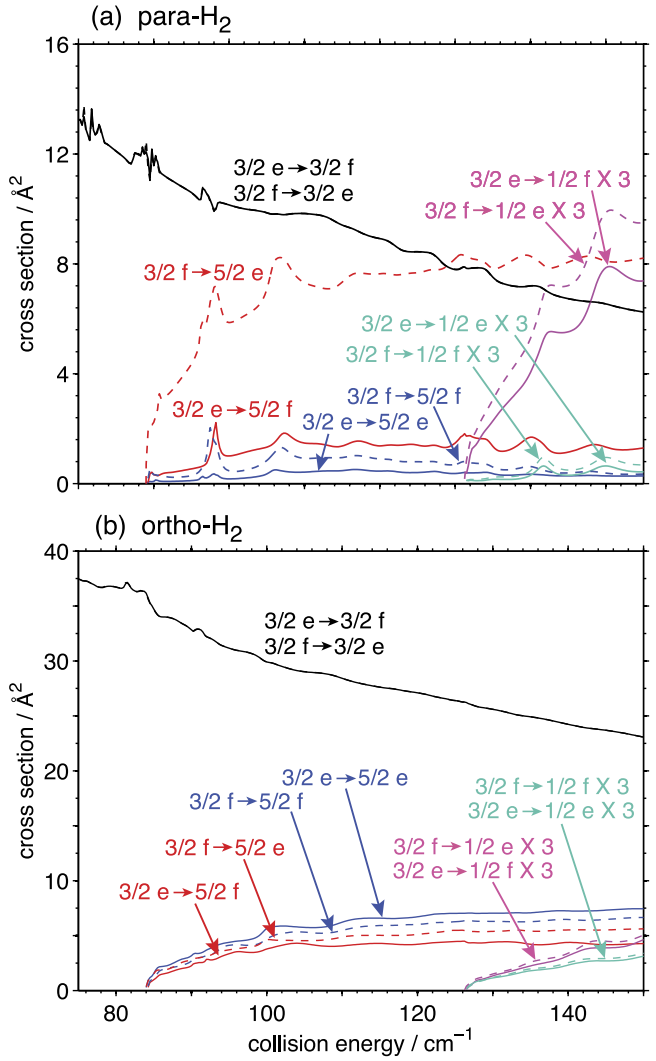

FIG. 14. Integral inelastic cross sections for collisions of the OH($X^2\Pi, j_1 = 3/2\ F_1e/f$) levels in collisions with (a) *p*-$H_2(j_2 = 0)$ and (b) *o*-$H_2(j_2 = 1)$ *vs.* collision energy over the range 75–150 cm^{-1}.

an important process since unequal Λ-doublet populations are generated in such collisions. We are hopeful that the present calculations will provide additional useful information for the modeling of laser pumping in the interstellar medium. As can be seen from Fig. 14, the cross sections for $e \rightarrow f$ and $f \rightarrow e$ transitions are quite different in magnitude. Hence, collision-induced transitions play a role in establishing the population inversion.

In Sec. III A, we showed that the OH–H_2 cross sections computed using our PES's differ significantly from those computed using the OvH PES's. This is particularly true for the collisions with *para*-H_2. Such difference signifies the inaccuracies in the OH–H_2 collisional (de-)excitation rate constants presently in use in various astrophysical applications. While astrophysical study is out of scope of this paper, our PES's,[24] scattering code,[39] and computed cross sections[36] are available and we encourage further study on this topic.

In this paper, we have reported measurements of state-to-state cross sections for transitions out of the OH($X^2\Pi, j_1 = 3/2\ F_1f$) level in collisions with *para*-, *ortho*-H_2 over the collision energy range 75–150 cm^{-1}. These experimental cross sections, as well as previous measurements by Schreel and ter Meulen[9] and Kirste *et al.*,[10] were compared with the results of quantum scattering calculations using the PES's computed by Ma *et al.*[24] The agreement of experiment and theory is generally very good. The principal discrepancy is in the relative magnitudes of the cross sections for transition to the $j_1' = 3/2\ F_1e$ and $j_1' = 5/2\ F_1e$ levels. As discussed previously[24] and in Sec. III B 1, improvement of the PES's will require extensive new *ab initio* calculations.

Notably, at collision energies near 93 cm^{-1}, theory predicts a slight rise, while experiment indicates a pronounced dip in the largest of the rotationally inelastic cross sections. This disagreement is not yet understood.

ACKNOWLEDGMENTS

M.H.A. and P.J.D. are grateful for support from the U.S. National Science Foundation (Grant No. CHE-1213332). Parts of the calculations were performed on the Deepthought cluster at the University of Maryland. A.v.d.A thanks the Alexander von Humboldt Foundation for a Senior Research Award. S.Y.T.v.d.M. acknowledges financial support from the Netherlands Organisation for Scientific Research through a VIDI grant and from the European Research Council through a Starting Grant. X.W. acknowledges the Alexander von Humboldt Foundation for a research fellowship. H.C.S. thanks Kopin Liu for fruitful discussions.

[1]I. Glassman and R. A. Yetter, *Combustion*, 4th ed. (Elsevier, 2008).
[2]*Gas-Phase Combustion Chemistry*, edited by W. C. Gardiner (Springer, 2000).
[3]R. P. Wayne, *Chemistry of Atmospheres*, 3rd ed. (Oxford University Press, 2000).
[4]E. Roueff and F. Lique, Chem. Rev. **113**, 8906 (2013).
[5]R. Atkinson, D. Baulch, R. Cox, J. Crowley, R. Hampson, R. Hynes, M. Jenkin, M. Rossi, and J. Troe, Atmos. Chem. Phys. **4**, 1461 (2004).
[6]G. Sarma, S. Marinakis, J. J. ter Meulen, D. H. Parker, and K. G. McKendrick, Nat. Chem. **4**, 985 (2012).
[7]P. Andresen, D. Haüsler, and H. W. Lülf, J. Chem. Phys. **81**, 571 (1984).
[8]P. Andresen, N. Aristov, V. Beushausen, D. Haüsler, and H. W. Lülf, J. Chem. Phys. **95**, 5763 (1991).
[9]K. Schreel and J. J. ter Meulen, J. Chem. Phys. **105**, 4522 (1996).
[10]M. Kirste, L. Scharfenberg, J. Kłos, F. Lique, M. H. Alexander, G. Meijer, and S. Y. T. van de Meerakker, Phys. Rev. A **82**, 042717 (2010).
[11]L. Scharfenberg, H. Haak, G. Meijer, and S. Y. T. van de Meerakker, Phys. Rev. A **79**, 023410 (2009).
[12]D. P. Dewangan and D. R. Flower, J. Phys. B **14**, 2179 (1981).
[13]D. P. Dewangan and D. R. Flower, J. Phys. B **16**, 2157 (1984).
[14]R. Schinke and P. Andresen, J. Chem. Phys. **81**, 5644 (1984).
[15]D. P. Dewangan, D. R. Flower, and G. Danby, J. Phys. B **19**, L747 (1986).
[16]D. P. Dewangan, D. R. Flower, and M. H. Alexander, Mon. Not. R. Astron. Soc. **226**, 505 (1987).
[17]G. C. Corey and M. H. Alexander, J. Chem. Phys. **88**, 6931 (1988).
[18]A. Offer and D. R. Flower, J. Phys. B: At., Mol. Opt. Phys. **23**, L391 (1990).
[19]A. R. Offer, M. C. van Hemert, and E. F. van Dishoeck, J. Chem. Phys. **100**, 362 (1994).
[20]S. M. Miller, D. C. Clary, A. Kliesch, and H.-J. Werner, Mol. Phys. **83**, 405 (1994).
[21]D. C. Clary, J. Phys. Chem. **98**, 10678 (1994).
[22]A. R. Offer and M. C. van Hemert, J. Chem. Phys. **99**, 3836 (1993).
[23]E. Kochanski and D. R. Flower, Chem. Phys. **57**, 217 (1981).
[24]Q. Ma, J. Kłos, M. H. Alexander, A. van der Avoird, and P. J. Dagdigian, J. Chem. Phys. **141**, 174309 (2014).
[25]R. A. Loomis, R. L. Schwartz, and M. I. Lester, J. Chem. Phys. **104**, 6984 (1996).

[26]K. B. Gubbels, Q. Ma, M. H. Alexander, P. J. Dagdigian, D. Tanis, G. C. Groenenboom, A. van der Avoird, and S. Y. T. van de Meerakker, J. Chem. Phys. **136**, 144308 (2012).
[27]A. B. Henson, S. Gersten, Y. Shagam, J. Narevicius, and E. Narevicius, Science **338**, 234 (2012).
[28]S. Chefdeville, Y. Kalugina, S. Y. T. van de Meerakker, C. Naulin, F. Lique, and M. Costes, Science **341**, 1094 (2013).
[29]L. Scharfenberg, J. Kłos, P. J. Dagdigian, M. H. Alexander, G. Meijer, and S. Y. T. van de Meerakker, Phys. Chem. Chem. Phys. **12**, 10660 (2010).
[30]L. Scharfenberg, K. B. Gubbels, M. Kirste, G. C. Groenenboom, A. van der Avoird, G. Meijer, and S. Y. T. van de Meerakker, Eur. Phys. J. D **65**, 189 (2011).
[31]M. Kirste, X. Wang, H. C. Schewe, G. Meijer, K. Liu, A. van der Avoird, L. M. C. Janssen, G. C. Gubbels, K. B. Groenenboom, and S. Y. T. van de Meerakker, Science **338**, 1060 (2012).
[32]J. M. Brown, J. T. Hougen, K.-P. Huber, J. W. C. Johns, I. Kopp, H. Lefebvre-Brion, A. J. Merer, D. A. Ramsay, J. Rostas, and R. N. Zare, J. Mol. Spectrosc. **55**, 500 (1975).
[33]S. Y. T. van de Meerakker, N. Vanhaecke, H. L. Bethlem, and G. Meijer, Phys. Rev. A **71**, 053409 (2005).
[34]M. Hillenkamp, S. Keinan, and U. Even, J. Chem. Phys. **118**, 8699 (2003).
[35]S. Pratt, P. Dehmer, and J. Dehmer, Chem. Phys. Lett. **105**, 28 (1984).
[36]See supplementary material at http://dx.doi.org/10.1063/1.4921562 for the technical details on the characterization of the H_2 beams, the calibration of the collision energy, and the comparison of signal intensities, as well as comparison of computed relative cross sections with those measured by Schreel and ter Meulen.
[37]H. L. Bethlem, F. M. H. Crompvoets, R. T. Jongma, S. Y. T. van de Meerakker, and G. Meijer, Phys. Rev. A **65**, 053416 (2002).
[38]G. C. Groenenboom, A. V. Fishchuk, and A. van der Avoird, J. Chem. Phys. **131**, 124307 (2009).
[39]HIBRIDON is a package of programs for the time-independent quantum treatment of inelastic collisions and photodissociation written by M. H. Alexander, D. E. Manolopoulos, H.-J. Werner, B. Follmeg, P. J. Dagdigian, and others. More information and/or a copy of the code can be obtained from the website http://www2.chem.umd.edu/groups/alexander/hibridon.
[40]K. P. Huber and G. Herzberg, *Molecular Spectra and Molecular Structure. IV. Constants of Diatomic Molecules* (Van Nostrand Reinhold, New York, 1979), http://webbook.nist.gov.
[41]F. Mélen, A. J. Sauval, N. Grevesse, C. B. Farmer, Ch. Servais, L. Delbouille, and G. Roland, J. Mol. Spectrosc. **174**, 490 (1995).
[42]T. Oka, Adv. At. Mol. Phys. **9**, 127 (1973).
[43]M. Kállay, Z. Rolik, I. Ladjánszki, L. Szegedy, B. Ladóczki, J. Csontos, and B. Kornis, Mrcc, a quantum chemical program suite, www.mrcc.hu; Z. Rolik, L. Szegedy, I. Ladjánszki, B. Ladóczki, and M. Kállay, J. Chem. Phys. **139**, 094105 (2013).
[44]L. Scharfenberg, S. Y. T. van de Meerakker, and G. Meijer, Phys. Chem. Chem. Phys. **13**, 8448 (2011).
[45]S. P. Walch and T. H. Dunning, J. Chem. Phys. **72**, 1303 (1980).
[46]G. C. Schatz and H. Elgersma, Chem. Phys. Lett. **73**, 21 (1980).
[47]M. H. Alexander, Chem. Phys. **92**, 337 (1985).
[48]M. H. Alexander, J. Chem. Phys. **76**, 5974 (1982).
[49]P. J. Dagdigian, M. H. Alexander, and K. Liu, J. Chem. Phys. **91**, 839 (1989).
[50]D. R. Flower, Phys. Rep. **174**, 1 (1989).
[51]N. D. Kylafis and C. A. Norman, Astrophys. J. **350**, 209 (1990).
[52]R. Cesaroni and C. M. Walmsley, Astron. Astrophys. **241**, 537 (1991).
[53]R. C. Doel, M. D. Gray, D. Field, and K. N. Jones, Astron. Astrophys. **280**, 592 (1993).